



# Effect of Sn-doping on the electrochemical behaviour of TiO<sub>2</sub> nanotubes as potential negative electrode materials for 3D Li-ion micro batteries

N.A. Kyeremateng<sup>a</sup>, F. Vacandio<sup>b</sup>, M.-T. Sougrati<sup>c</sup>, H. Martinez<sup>d</sup>, J.-C. Jumas<sup>c</sup>, P. Knauth<sup>b</sup>, T. Djenizian<sup>a,\*</sup>

<sup>a</sup> Aix Marseille Université, CNRS, LP3 UMR 7341, 13288, Marseille, France

<sup>b</sup> Aix Marseille Université, CNRS, MADIREL, UMR 7246, 13397, Marseille, France

<sup>c</sup> Institut Charles Gerhardt, CNRS UMR5253, Université Montpellier 2, 34095 Montpellier, France

<sup>d</sup> Laboratoire IPREM – UMR 5254, Université de Pau et des Pays de l'Adour, Hélioparc Pau-Pyrénées, 2 Av du Président Angot, 64053 Pau Cedex 9, France

## HIGHLIGHTS

- ▶ Sn-doped TiO<sub>2</sub> nanotubes were fabricated by anodization of sputtered Ti–Sn thin films.
- ▶ The Sn-doped TiO<sub>2</sub>nts can be used as anodes for 3D Li-ion micro batteries.
- ▶ The electrochemical performance of Sn-doped TiO<sub>2</sub>nts was better than simple TiO<sub>2</sub>nts.
- ▶ The improved performance is related to enhanced lithium diffusivity with Sn doping.
- ▶ This synthesis approach is extendable for Fe/Sb/Nb-doping of TiO<sub>2</sub> nanotubes.

## ARTICLE INFO

### Article history:

Received 19 June 2012

Received in revised form

1 August 2012

Accepted 30 September 2012

Available online 6 October 2012

### Keywords:

Titanium nanotubes

Mössbauer spectroscopy

Co-sputtering

Anodization

Lithium

Micro batteries

## ABSTRACT

Self-organized Sn-doped TiO<sub>2</sub> nanotubes were fabricated by anodization of co-sputtered Ti–Sn thin films in a glycerol electrolyte containing NH<sub>4</sub>F. The Sn-doped TiO<sub>2</sub>nts were studied in terms of composition, morphology and structure by scanning electron microscopy, X-ray diffraction, X-ray photoelectron spectroscopy and <sup>119</sup>Sn Mössbauer spectroscopy. The electrochemical behaviour of the Sn-doped TiO<sub>2</sub>nts was evaluated in Li test cells as a possible negative electrode for 3D Li-ion micro batteries. The Sn-doped TiO<sub>2</sub>nts delivered much higher capacity values compared to simple TiO<sub>2</sub>nts. The outstanding electrochemical behaviour is proposed to be related to the enhanced lithium diffusivity evidenced with Cottrell plots, and the rutile-type structure imparted with the Sn doping.

© 2012 Elsevier B.V. All rights reserved.

## 1. Introduction

The advent of modern microelectronic devices challenges scientists to investigate high-performance micro batteries. All-solid-state (thin-film) micro batteries are integrated into micro-electronic circuit boards to deliver low energy to various devices such as hearing aids, medical implants, remote sensors, RFID tags etc [1–3].

To date, these micro batteries are based on a parallel (or pseudo-parallel) or a sandwich configuration of planar electrodes separated

by a solid electrolyte. This planar configuration leads to relatively low volumetric energy and power densities. However, the miniaturization of recent electronic devices requires higher volumetric energy densities in addition to size diminution (on the order of 0.1 cm<sup>3</sup>). In this context, the development of three-dimensional (3D) thin-film micro batteries represents a viable alternative [4,5]. The 3D design will ensure that anode and cathode materials have (active) surface areas exposed in three dimensions – exploiting the out-of-plane dimension instead of just the conventional in-plane surface. Nano-structuration of electrode materials is one of the most promising approaches to realize this 3D paradigm of micro batteries [6]. Not only is the reduction of the areal footprint crucial, new and highly performing anode, cathode and electrolyte materials are also imperative for high performance and low manufacturing cost.

\* Corresponding author. Tel.: +33 786 000 028; fax: +33 491 829 289.

E-mail address: [Thierry.djenizian@univ-amu.fr](mailto:Thierry.djenizian@univ-amu.fr) (T. Djenizian).

Actually, the negative electrode material of thin-film micro batteries is of a great concern. Almost all thin-film micro batteries utilize metallic lithium anode that has a low melting point and a strong reactivity. Furthermore, an expensive packaging technology is always required due to the lithium anode [7,8]. Recently, significant attempts are being made to fully adopt the “Li-ion” or the “rocking-chair” concept in the design of lithium-based micro batteries [1,9]. This implies combining cathode materials such as  $\text{LiCoO}_2$ ,  $\text{LiMn}_2\text{O}_4$  or  $\text{LiFePO}_4$  [10–12] with the wide range of possible anode materials proven to react reversibly with lithium either by insertion [13,14], alloying [9,15–18] or conversion [19–22]. Cathode materials such as  $\text{V}_2\text{O}_5$  and  $\text{TiO}_x\text{S}_y$  are of considerable interest particularly with a lithiated anode material to maintain the ‘Li-ion’ concept [8,23–25]. Among all the potential anode materials,  $\text{TiO}_2$  nanotubes ( $\text{TiO}_2\text{nts}$ ) possess a spectacular characteristic for the design of 3D Li-ion micro batteries [26,27]. Besides the self-organized (3D) nano-architecture,  $\text{TiO}_2$  nanotubes exhibit very good capacity retention particularly at moderately high kinetic rates [13,14,27–29]. As  $\text{TiO}_2$  (anatase or rutile) effectively inserts only 0.5  $\text{Li}^+$  per formula unit, corresponding to a theoretical capacity of 168  $\text{mAh g}^{-1}$  [14,30,31], interest has risen recently to improve the overall performance of  $\text{TiO}_2$  nanotubes for the design of high-performance 3D Li-ion micro batteries.  $\text{TiO}_2$  being a semiconductor, selective doping by aliovalent or homovalent substitution of Ti affects the intrinsic electrical properties to some extent.

In this work,  $\text{TiO}_2$  nanotubes were doped with  $\text{Sn}^{4+}$  by potentiostatic anodization of Ti–Sn thin films which were produced by co-sputtering of titanium and tin targets. X-ray diffraction, X-ray photoelectron spectroscopy and  $^{119}\text{Sn}$  Mössbauer spectroscopy were employed to help ascertain the quality of the doping operation. The effects of  $\text{Sn}^{4+}$  doping on the morphology and the electronic properties of  $\text{TiO}_2$  nanotubes were investigated. Finally, the impact of  $\text{Sn}^{4+}$  doping on the electrochemical behaviour of  $\text{TiO}_2$  nanotubes as anodes for 3D Li-ion micro batteries was evaluated in lithium test cells.

## 2. Experiment

Metallic targets (Ti and Sn, 99.9% pure) were supplied by Sigma–Aldrich. For the co-sputtering, the Ti and Sn targets were cut into the right proportions (considering the sputtering rates of Ti and Sn in relation to the anticipated thin film composition), cleaned and assembled in a target holder with the aid of a silver paste. The target, after drying overnight at room temperature, was inserted into the PVD chamber. Silicon substrates (p-type Si with a resistivity of 1–10  $\Omega \text{ cm}$  [WaferWorld, Inc.]) were cut to size along the (100) crystallographic plane and cleaned by sonicating sequentially in acetone, isopropanol, and methanol for 10 min each. The native oxide layer was then removed by dipping the Si wafers in a solution of 1 wt% HF for 1 min, followed by rinsing with distilled water and drying with compressed air. The cleaned Si substrates were immediately inserted into the PVD chamber which was subsequently evacuated until a low residual pressure was reached ( $10^{-6}$  mbar).

Thin films (Ti or Ti–Sn) of  $\sim 1.5 \mu\text{m}$  thickness were deposited by cathodic sputtering onto the mirror-polished Si wafers. The substrates were constantly rotated ( $360^\circ$ ) during the deposition to ensure a uniform thin film composition. An ultrapure Ar atmosphere was maintained inside the chamber at a pressure of  $6 \times 10^{-4}$  mbar during the deposition, with a current of 150 mA. For the Ti–Sn thin film, Ti was first deposited for 30 min to obtain a barrier layer on the silicon substrate for galvanostatic experiments. Anodization experiments were carried out by applying a constant voltage of 40 V during 1.5 h in a conventional two electrode cell using an EG&G PARSTAT 2273 potentiostat/

galvanostat. The thin films (Ti or Ti–Sn) were the working electrodes while a platinum foil served as a counter electrode. The electrodes were separated by a distance of 3 cm and the electrolyte was a solution of 88.7 wt% glycerol, 1.3 wt%  $\text{NH}_4\text{F}$  and 10 wt%  $\text{H}_2\text{O}$ .

Optional thermal treatments at 450  $^\circ\text{C}$  were performed in air during 3 h. X-ray-diffraction studies were carried-out at room temperature with a step-time of 10 s and step-size of  $0.02^\circ$  using a Siemens D5000 diffractometer with  $\text{Cu K}\alpha$  radiation ( $\lambda = 1.5406 \text{ \AA}$ ). Scanning Electron Microscope (SEM) images were recorded with a Philips XL-30 FEG SEM. Mott–Schottky analysis was carried out in a 0.1 M  $\text{Na}_2\text{SO}_4$  solution using an Ag/AgCl reference electrode, a platinum foil counter electrode and the nanotubes as working electrodes. The potential was changed in 0.1 V voltage steps and the impedance was determined at 30 Hz fixed frequency with 10 mV a.c. amplitude using an EG&G PARSTAT 2273 potentiostat/galvanostat.

$^{119}\text{Sn}$  room temperature Mössbauer spectra were recorded in the constant acceleration mode and Conversion Electron Mössbauer Spectroscopy (CEMS) geometry. A specific helium-flow counter was used for the detection of conversion electrons. The  $\gamma$ -ray source consisted of  $\text{Ba}^{119\text{m}}\text{SnO}_3$  with a nominal activity of 7 mCi. The hyperfine parameters, isomer shift ( $\delta$ ) and quadrupole splitting ( $\Delta$ ), were determined by fitting appropriate Lorentzian lines to the experimental data. The quality of the fit was controlled by the usual  $\chi^2$ -test. All isomer shifts for Sn are given relative to  $\text{BaSnO}_3$  at room temperature.

XPS measurements were carried out with a Kratos Axis Ultra spectrometer, using focused monochromatized Al  $\text{K}\alpha$  radiation ( $h\nu = 1486.6 \text{ eV}$ ). The XPS spectrometer was directly connected to an argon dry box through a transfer chamber, to avoid moisture/air exposure of the samples. The analysed area of the samples was  $300 \mu\text{m} \times 700 \mu\text{m}$ . Peaks were recorded with a constant pass energy of 20 eV. The pressure in the analysis chamber was around  $5 \times 10^{-8}$  Pa. Short acquisition time spectra were recorded before and after each normal experiment to check that the samples did not suffer from degradation under the X-ray beam during measurements. Peak assignments were made with respect to experimental reference compounds, namely bulk anatase and/or rutile  $\text{TiO}_2$ . The binding energy scale was calibrated from hydrocarbon contamination using the C1s peak at 285.0 eV. Core peaks were analysed using a non-linear Shirley-type background. The peak positions and areas were optimized by a weighted least-square fitting method using 70% Gaussian and 30% Lorentzian line-shapes. Quantification was performed on the basis of Scofield’s relative sensitivity factors.

For the electrochemical measurements, two-electrode Swagelok-type cells were assembled in a glove-box filled with purified argon in which moisture and oxygen contents were less than 2 ppm. The galvanostatic experiments were then carried out with the prepared  $\text{Li/LiPF}_6$  (EC:DEC)/ $\text{W}_E$  (Working electrode) cells using a VersaSTAT 3 potentiostat/galvanostat. The electrolyte supplied by Merck was embedded in a Whatman glass microfiber, which acts as a separator. It is remarkable to note that additives such as poly(vinyl difluoride) that is a binding agent, and carbon black (conductive agent) were not utilized. For the discharge/charge, a constant current density of  $70 \mu\text{A cm}^{-2}$  (1C) was applied to the assembled cells in the  $1.0 \leq U/V \leq 2.6$  voltage range. Additionally, cyclic voltammetry was carried out with the VersaSTAT 3 potentiostat/galvanostat in the  $0.65 \leq U/V \leq 3$  voltage range at a scan rate of  $0.1 \text{ mV s}^{-1}$ .

## 3. Results and discussion

### 3.1. Morphology, composition and structure

Fig. 1 shows the current transients recorded during the anodization of Ti and Ti–Sn thin films in an electrolyte consisting of 88.7 wt% glycerol, 1.3 wt%  $\text{NH}_4\text{F}$  and 10 wt%  $\text{H}_2\text{O}$ . It can clearly be

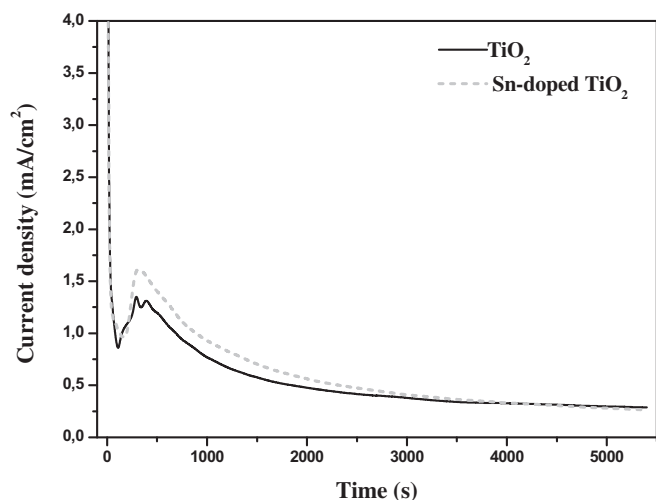


**Fig. 1.** Chronoamperometric curves obtained during the anodization of Ti and Ti–Sn thin films at 40 V in an electrolyte consisting of 88.7 wt% glycerol, 1.3 wt%  $\text{NH}_4\text{F}$  and 10 wt%  $\text{H}_2\text{O}$ .

noticed that both thin films exhibit the current-transient profile characteristic of nanotubes formation [13,32,33], that is, there is a sharp drop in the anodization current in the first 100 s due to the formation of an initial insulating oxide layer followed by an increase in the current due to the formation of pits in the oxide by a chemical dissolution effect of fluoride ions and the concomitant increase in surface area. The current then decreases as the pits grow into uniformly-spread pores over the surface and increase diffusion length for the reacting ionic species. Finally, the pores grow into nanotubes when the current becomes almost constant as a result of a competition between electrochemical oxide formation and chemical dissolution. The only drastic variation is that the Sn incorporation led to higher peak current values from  $t = 400$  to  $t = 3000$  s, and this can be explained as a consequence of the formation of smaller diameter Sn-doped  $\text{TiO}_2$  nanotubes.

The SEM images of the resulting nanotubes of  $\text{TiO}_2$  and Sn-doped  $\text{TiO}_2$  are given in Fig. 2. It can be emphasized that the silicon substrates were not heated during the sputtering process. Although the XRD patterns of sputtered Ti thin films previously studied [13,34,35] correspond to hexagonal titanium (JCPDS: 44-1294), we have recently reported that the Ti–Sn thin film corresponds to  $\text{Sn}_3\text{Ti}_5$  intermetallic [29] (JCPDS: 3-65-3605). The formation of the  $\text{Sn}_3\text{Ti}_5$  intermetallic is not unusual according to the Hume-Rothery rules, and by anodization under the same conditions as those adopted for the production of the  $\text{TiO}_2$  nanotubes

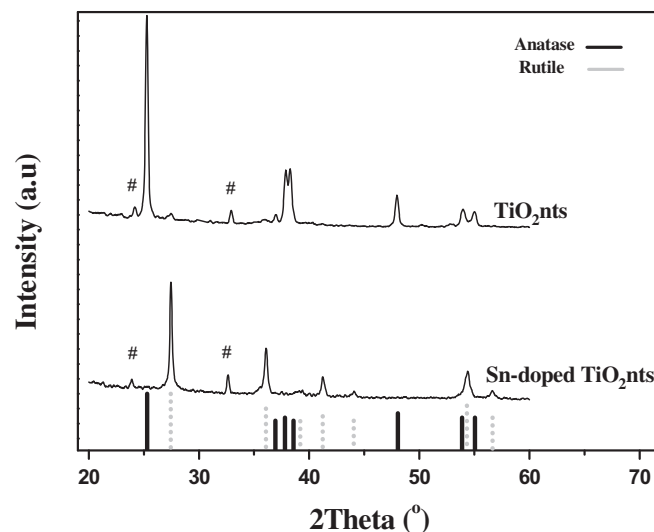


**Fig. 3.** X-ray diffractograms of  $\text{TiO}_2\text{nts}$  and Sn-doped  $\text{TiO}_2\text{nts}$  recorded after thermal treatments at 450 °C. The low intensity peaks marked '#' are emanating from the silicon substrate.

(Fig. 2b), highly-ordered Sn-doped  $\text{TiO}_2$  nanotubes (Fig. 2a) were obtained.

We have already demonstrated the possibility to grow Sn-doped  $\text{TiO}_2$  nanotubes by anodization of Ti–Sn thin films in aqueous electrolytes (1 M  $\text{H}_3\text{PO}_4$ , 1 M  $\text{NaOH}$  and 0.4 wt%  $\text{HF}$ ) [29]. Compared with these previous results, the morphology of the nanotubes is strongly influenced by the viscosity of the electrolyte as well as the content of water. As shown in Fig. 2, the undoped  $\text{TiO}_2$  nanotubes have lengths of  $\sim 1.4$   $\mu\text{m}$ , diameters of  $\sim 160$  nm, and sidewall thickness of  $\sim 20$  nm; whilst the Sn-doped  $\text{TiO}_2$  nanotubes have lengths of  $\sim 1.2$   $\mu\text{m}$ , diameters of  $\sim 120$  nm, and sidewall thickness of  $\sim 15$  nm.

Fig. 3 shows X-ray diffractograms of the nanotubes recorded after thermal treatments at 450 °C. It can be noticed that whilst the  $\text{TiO}_2\text{nts}$  crystallize (after the thermal treatment) in the anatase structure (JCPDS: 21-1272) with an infinitesimal rutile proportion (JCPDS: 21-1276), the Sn-doped  $\text{TiO}_2\text{nts}$  are transformed entirely into a rutile-type structure (JCPDS: 21-1276) without any traces of  $\text{SnO}_2$  (cassiterite) nor  $\text{SnO}$  (romarchite). This transformation from anatase to rutile observed for the  $\text{Ti}_{1-x}\text{Sn}_x\text{O}_2$ -type nanotubes is consistent with the already established fact that  $\text{Sn}^{4+}$  substitution for  $\text{Ti}^{4+}$  in  $\text{TiO}_2$  is generally accompanied by the structural transformation from anatase to rutile except for very low ( $x \leq 0.05$ ) Sn contents [36,37].

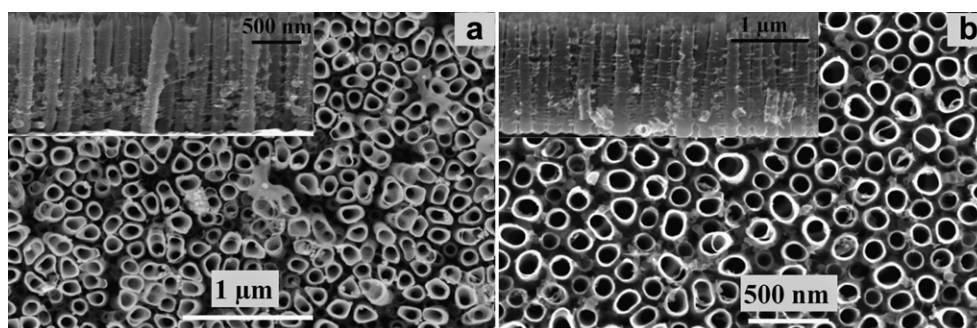


**Fig. 2.** SEM images of (a) Sn-doped  $\text{TiO}_2$  nanotubes (Inset: cross-section), and (b) undoped  $\text{TiO}_2$  nanotubes (Inset: cross-section) prepared at 40 V in the electrolyte consisting of 88.7 wt% glycerol, 1.3 wt%  $\text{NH}_4\text{F}$  and 10 wt%  $\text{H}_2\text{O}$ .

In order to confirm the oxidation state of the Sn dopants and ascertain the degree of the doping, X-ray photoelectron spectroscopy was carried out on the as-prepared TiO<sub>2</sub> nanotubes (analysed for comparison) and Sn-doped TiO<sub>2</sub> nanotubes. The obtained high-resolution Ti2p, O1s, C1s and Sn3d XPS core peaks are presented in Figs. 4 and 5. The corresponding data and quantitative analysis are given in Table 1. For both samples, carbon contamination was detected (arising from the traces of the solvent used for the anodization).

For the as-prepared TiO<sub>2</sub> nanotubes, the C1s spectrum presents one main component located at 285.0 eV, associated with C–C or C–H bonds; and two other components at about 286.5 and 288.9 eV, attributed to C–O and O=C–O bonds respectively. Quite similar attributions can be done for the Sn-doped TiO<sub>2</sub> nanotubes, except a very low intensity component located at a high binding energy (289.7 eV), which could correspond to a very low quantity of carbonate species. Due to spin-orbit coupling for both samples, each spectrum exhibits two main Ti2p components located at 459.0 eV (Ti2p<sub>3/2</sub>) and 464.7 eV (Ti2p<sub>1/2</sub>). These binding energies (B.E) are representative of Ti<sup>4+</sup> in an oxygen environment, which is in agreement with previous XPS data for bulk and thin film TiO<sub>2</sub> [38–42].

In addition, the spectra also contain distinct charge-transfer satellite peaks at about 13 eV above the 2p<sub>3/2</sub> and 2p<sub>1/2</sub> main peak positions. The origin of Ti2p satellite peaks is under debate [43–47]; one of the most likely explanations is the strong covalent hybridization between the metal d and the oxygen p orbitals [43]. The main peaks are essentially characterized by the well screened final state configuration:  $2p^5 3d^1 L^{-1}$ , where  $L$  denotes the ligand electron [44]. The satellite peaks are caused by the hole–particle pair “shake-up” excitation on the anions in the presence of the ligand–metal charge transfer screened core hole. They mostly correspond to the final state configurations  $2p^5 d^0$  and  $2p^5 d^1 L^{-1} L' L''^{-1}$  [45].

For both samples, the O1s core peaks also present three components. The first one, located at 530.4(5) eV, is assigned to oxygen atoms of the TiO<sub>2</sub> oxide lattice. Hence, it can be noted from Table 1 that for the as-prepared undoped TiO<sub>2</sub> nanotubes, the O/Ti atomic ratio is close to 2 (37.6/19.3); and for the as-prepared Sn-doped TiO<sub>2</sub> nanotubes, the O/(Ti + Sn) atomic ratio is also close to 2 (39.7/22.3). Certainly, the two other O1s core peaks (531.7 and 532.8 eV) are related to O=C–O and C–O bonds from solvent traces, in agreement with C1s core peaks. Obviously, the Sn doping does not seem to affect the ionic network of titanium dioxide nanotubes, as no substantial modifications of binding energies were observed. Owing to spin-orbit coupling effects, two peaks corresponding to Sn3d<sub>5/2</sub> (487.1 eV) and Sn3d<sub>3/2</sub> (495.5 eV), are

observed, which are ascribable to Sn<sup>4+</sup> incorporated into the TiO<sub>2</sub> lattice [48,49]. The quantity of the Sn dopants ( $x$ ) in the Ti<sub>1-x</sub>Sn<sub>x</sub>O<sub>2</sub>-type nanotubes was estimated to be  $\sim 0.5$ , since a Ti/Sn ratio of  $\sim 1$  was obtained (Table 1).

Fig. 6a–c presents the <sup>119</sup>Sn Mössbauer spectra of the Ti–Sn thin film, and the Sn-doped TiO<sub>2</sub>nts before and after annealing at 450 °C for 3 h. All these spectra were obtained under the same conditions. A summary of the obtained hyperfine parameters is given in Table 2. The parameters ( $\delta = 1.688(8)$  mm s<sup>−1</sup>;  $\Delta = 0.47(2)$  mm s<sup>−1</sup>) obtained for the signal of the Ti–Sn thin film (Fig. 6a) can be attributed to Sn<sup>0</sup>, emphasizing that the sputtering process led to pure metallic products. Moreover, the weak line width ( $2\Gamma$ ) of the Sn<sup>0</sup> signal is consistent with the XRD results that the Ti–Sn thin film does not consist of a mixture of phases. Although the starting Ti–Sn thin film corresponds (according to X-ray Diffraction) to Sn<sub>3</sub>Ti<sub>5</sub> intermetallic as mentioned earlier, the <sup>119</sup>Sn Mössbauer spectroscopy studies could not confirm the exact nature of this thin film as the hyperfine parameters did not exactly match those of Ti–Sn intermetallics previously reported [50,51]. However, Ti<sub>2</sub>Sn ( $\delta = 1.76$  mm s<sup>−1</sup>), Ti<sub>3</sub>Sn ( $\delta = 1.80$  mm s<sup>−1</sup>) and Ti<sub>5</sub>Sn<sub>3</sub> ( $\delta = 1.81$  mm s<sup>−1</sup>) have isomer shifts close to what was obtained for our Ti–Sn thin film although the quadrupole splitting of the former intermetallics were more intense [50,51]. It is important to note that the intermetallics mentioned in literature, apart from having particulate morphologies, were produced by arc melting and annealed at very high temperatures. In addition, XRD evidenced the presence of impurity phases [50,51]. Thus the mismatch in the hyperfine parameters in comparison to the present results can be explained by the differences in synthesis routes, thermal treatments, morphologies, and purity of the crystalline phases.

The spectrum of the as-prepared Sn-doped TiO<sub>2</sub>nts (Fig. 6b) consists of two unresolved doublets. The doublet at  $\delta = 1.66(3)$  mm s<sup>−1</sup> is attributed to the Sn<sup>0</sup> from the remaining Ti–Sn layer that has not been anodized. Although the presence of this un-anodized Ti–Sn layer was not revealed by XRD, it can be due to the fact that, most probably, the amount of the remaining Ti–Sn layer is below the detection limit of XRD. This is consistent with the undoped TiO<sub>2</sub> nanotubes; the presence of un-anodized Ti layer was also not revealed by XRD. The other doublet at  $\delta = 0.06(2)$  mm s<sup>−1</sup> can be ascribed to Sn(IV). The isomer shift of  $\delta = 0.06(2)$  is very close to what is typically obtained for Sn(IV) bonded to oxygen in octahedral environments [52–54]. These Mössbauer parameters are also in good agreement with those previously [55] obtained for Sn-doped anatase TiO<sub>2</sub> particles. The structural and chemical characterization performed by XRD, XPS, and Mössbauer spectroscopy clearly confirm the octahedral substitution of Sn<sup>4+</sup> for Ti<sup>4+</sup> in the self-organized TiO<sub>2</sub> nanotubes.

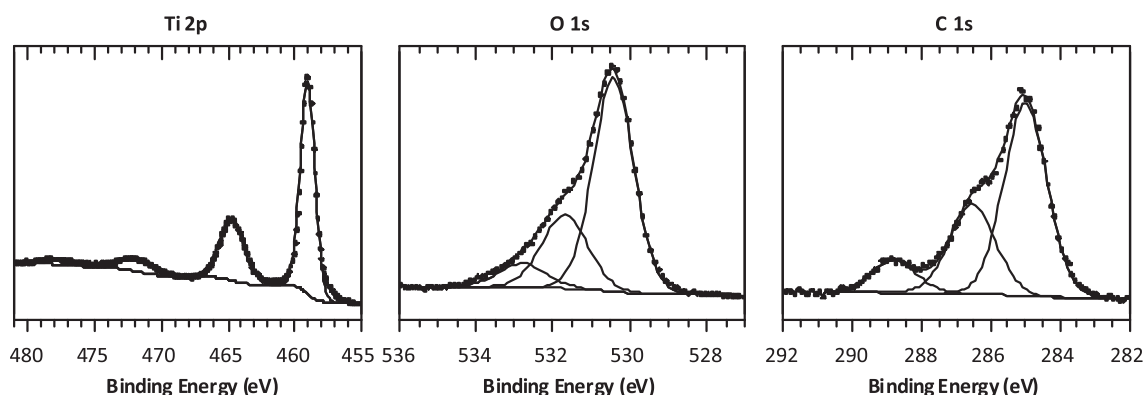


Fig. 4. High-resolution Ti2p, O1s and C1s XPS spectra for the as-prepared TiO<sub>2</sub> nanotubes.

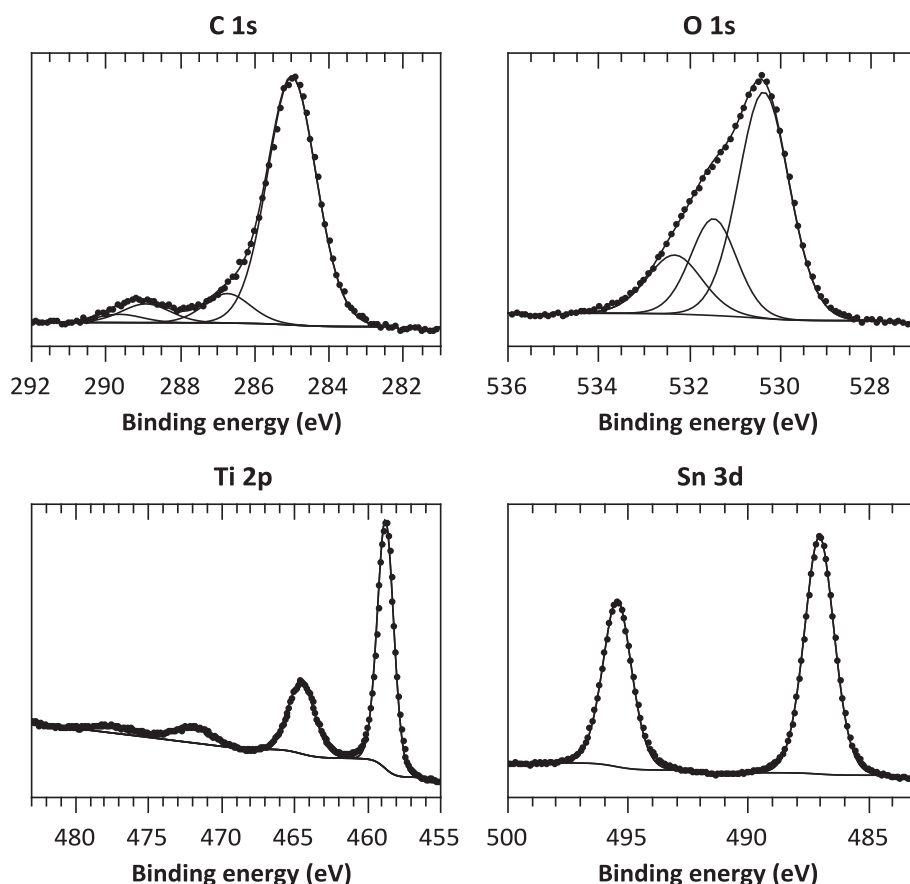


Fig. 5. High-resolution Ti2p, O1s, C1s and Sn3d XPS spectra for the as-prepared Sn-doped TiO<sub>2</sub> nanotubes.

When the Sn-doped TiO<sub>2</sub>nts sample is annealed (Fig. 6c), two modifications are observed: (i) the intensity of the emission signal increased, indicating that annealing induced an increase in crystallite size; and (ii) the quadrupole splitting of the Sn<sup>4+</sup> doublet decreased, indicating a better ordered lattice for the annealed sample. The relative amounts of Sn<sup>0</sup> and Sn<sup>4+</sup> were not significantly affected by the heat treatment. Moreover, the Sn<sup>0</sup> doublet has the

Table 1

Binding energies, full widths at half maximum (FWHM) and atomic percentages of Ti2p, O1s, C1s and Sn3d XPS core peaks for the as-prepared TiO<sub>2</sub> and Sn-doped TiO<sub>2</sub> nanotubes. The italicized numbers are the total at% of the contributions to the different core peaks.

Core peaks	TiO <sub>2</sub>			Sn-doped TiO <sub>2</sub>		
	B.E. (eV)	FWHM	at%	B.E. (eV)	FWHM	at%
C1s	285.0	1.4	18.3	285.0	1.5	21.8
	286.5	1.5	6.3	286.6	1.5	3.7
	288.8	1.5	2.8	288.9	1.5	2.8
				289.8	1.5	0.8
			27.4			29.1
Ti2p	459.0	1.3	10.9	458.8	1.3	6.6
	464.7	2.2	5.8	464.5	2.1	3.1
	471.9	3.2	1.8	472.0	3.2	1.0
	477.6	3.4	0.8	477.5	3.0	0.4
			19.3			11.1
O1s	530.4	1.2	37.6	530.5	1.2	39.7
	531.7	1.4	11.4	531.6	1.3	7.0
	532.8	1.4	4.5	532.7	1.4	4.4
			53.3			49.1
Sn3d				487.1	1.4	6.7
				495.5	1.4	4.5
						11.2

same parameters as those obtained for the as-prepared Sn-doped TiO<sub>2</sub>nts sample and the as-sputtered Ti–Sn thin film, indicating that the structure of the Ti–Sn thin film is conserved for all samples.

### 3.2. Electronic properties

From the Mott–Schottky equation given in Eq. (1), the flat band potential ( $E_{fb}$ ) and the charge carrier concentration ( $N_D$ ) of a specific semiconductor can be determined by plotting  $C^{-2}$  versus  $E$  (potential).

$$\frac{1}{C^2} = \left( \frac{2}{q\epsilon\epsilon_0 N_D} \right) \left( E - E_{fb} - \frac{kT}{q} \right) \quad (1)$$

Where  $C$  is the capacitance of the space charge layer;  $q$  the elementary charge ( $1.6 \times 10^{-19}$  C);  $\epsilon_0$  the vacuum permittivity ( $8.85 \times 10^{-14}$  F cm<sup>-1</sup>);  $\epsilon$  the dielectric constant of the studied semiconductor;  $k$  is Boltzmann's constant; and  $T$  is the absolute temperature. Fig. 7 shows the Mott–Schottky plots obtained for the undoped and the Sn-doped TiO<sub>2</sub>nts. The positive slope of each plot is in agreement with n-type semi-conductivity. In principle, TiO<sub>2</sub> tends to be oxygen-deficient at ambient temperature and pressure, making the material an n-type semiconductor according to the defect equilibrium given below in Kröger–Vink notation:



For both undoped and Sn-doped TiO<sub>2</sub>nts, approximately the same values of  $E_{fb}$  (−0.85 V vs Ag/AgCl) and  $N_D$  ( $6.5 \times 10^{19}$  cm<sup>-3</sup>)

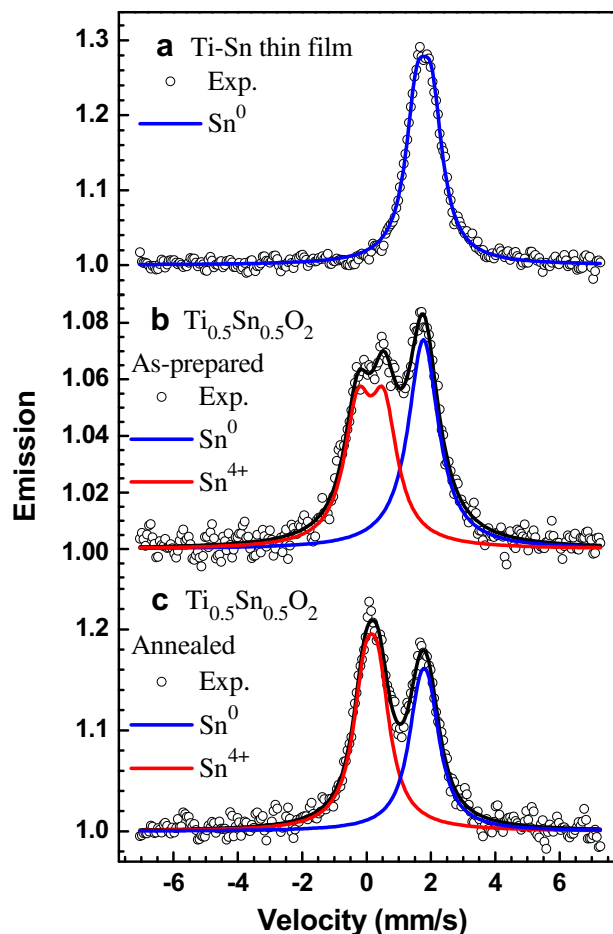


**Fig. 6.** Room temperature  $^{119}\text{Sn}$  Mössbauer spectra recorded for as-deposited Ti–Sn thin film (a), and Sn-doped  $\text{TiO}_2$ nts (b: amorphous, c: annealed at  $450^\circ\text{C}$ ).

were estimated, which is consistent with the theoretical consideration that  $\text{Sn}^{4+}$  substitution for  $\text{Ti}^{4+}$  (isovalent) in  $\text{TiO}_2$  should not modify the semi-conducting behaviour.

The conductivity ( $\sigma$ ) of either the undoped or the Sn-doped  $\text{TiO}_2$ nts can be estimated using the charge carrier concentration ( $N_i$ ), the electron mobility ( $\mu_i$ ) and the elementary charge ( $q_i$ ) according to Eq. (3) [56,57]; but the resulting values should be indistinguishable as the same values of charge carrier concentration ( $N_i$ ) were obtained from the Mott–Schottky analysis.

$$\sigma_i = q_i \mu_i N_i \quad (3)$$

However, it has previously [36] been demonstrated that  $\text{Sn}^{4+}$  substitution for  $\text{Ti}^{4+}$  in  $\text{TiO}_2$  leads to increase of the bond lengths of the inner coordination shells due to the larger ionic radius of  $\text{Sn}^{4+}$

**Table 2**

Room temperature  $^{119}\text{Sn}$  Mössbauer hyperfine parameters obtained from Ti–Sn thin film, as-prepared and annealed Sn-doped  $\text{TiO}_2$ nts.

Sample	Attribution	$\delta$ (mm/s)	$\Delta$ (mm/s)	$2I$ (mm/s)	$C$ (%)	$\chi^2$
Ti–Sn thin film	$\text{Sn}^0$	1.688(8)	0.47(2)	0.84(2)	100	0.42
As-prepared	$\text{Sn}^0$	1.66(3)	0.36(6)	0.98(7)	46(8)	0.46
Sn-doped $\text{TiO}_2$ nt	$\text{Sn}^{4+}$	0.05(2)	0.81(2)	1.02(5)	54(6)	
Annealed	$\text{Sn}^0$	1.69(2)	0.32(8)	0.91(6)	43(1)	0.51
Sn-doped $\text{TiO}_2$ nt	$\text{Sn}^{4+}$	0.06(2)	0.42(5)	0.91(6)	57(1)	

$\delta$ : isomer shift;  $\Delta$ : quadrupole splitting;  $2I$ : full line width at half-maximum;  $C$ : contribution to total emission (not corrected due to unknown Lamb–Mössbauer factors);  $\chi^2$ : goodness of the fitting.

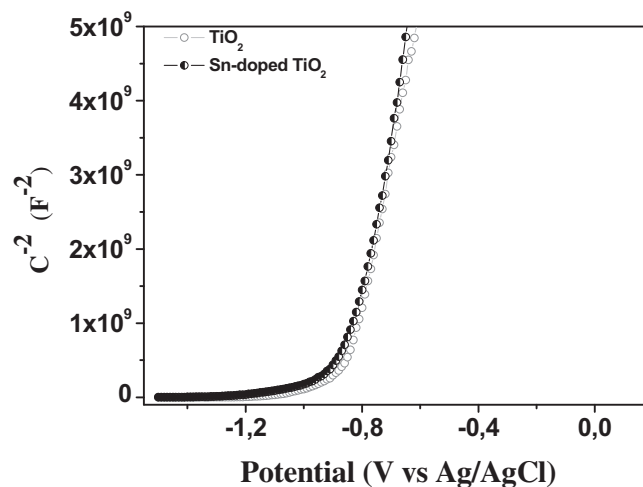


**Fig. 7.** Mott–Schottky plots obtained for the undoped and the Sn-doped  $\text{TiO}_2$ nts in a 0.1 M  $\text{Na}_2\text{SO}_4$  solution at 30 Hz.

[ $r(\text{Sn}^{4+}) = 0.83 \text{ \AA}$ ] compared to  $\text{Ti}^{4+}$  [ $r(\text{Ti}^{4+}) = 0.75 \text{ \AA}$ ]. Fundamentally, increased bond lengths are indicative of weakened bonds and thus migration of cations ( $\text{Li}^+$ ) is expected to be enhanced in the modified lattice. In view of this, we carried out potentiostatic experiments for which the current-transient profiles before the onset of a limiting current can be described by the Cottrell equation [58,59]:

$$j = nFD_0^{1/2}C_0\pi^{-1/2}t^{-1/2} \quad (4)$$

The potentiostatic experiments consisted of applying a potential step (from 3.0 to 1.4 V vs  $\text{Li}^+/\text{Li}$ ) to cells of  $\text{Li}/\text{LiPF}_6$  (EC:DEC)/( $\text{TiO}_2$ nts or Sn-doped  $\text{TiO}_2$ nts) during 30 s. Assuming the composition of the initial subsurface layer to be  $\text{Li}_{0.5}\text{TiO}_2$  for both  $\text{TiO}_2$ nts and Sn-doped  $\text{TiO}_2$ nts, the concentration of  $\text{Li}^+$  ( $C_0$ ) was calculated to be  $25 \times 10^{-3} \text{ mol cm}^{-3}$  using  $4 \text{ g cm}^{-3}$  density of  $\text{TiO}_2$ . Hence, the diffusion coefficients ( $D_0$ ) were estimated from the slopes of the fits to the Cottrell plots (Fig. 8) to be  $1.6 \times 10^{-13} \text{ cm}^2 \text{ s}^{-1}$  and  $6.7 \times 10^{-12} \text{ cm}^2 \text{ s}^{-1}$  for  $\text{TiO}_2$ nts and Sn-doped  $\text{TiO}_2$ nts respectively. These values of diffusion coefficients agree with previous reports [58,59] in literature and indicate that  $\text{Li}^+$  insertion into Sn-doped  $\text{TiO}_2$ nts is about 40 times faster than into undoped  $\text{TiO}_2$ nts. This is consistent with the assertion that increased bond lengths lead to more easy lithium ion diffusion in the structure.

### 3.3. Electrochemical behaviour versus lithium

The electrochemical behaviour versus lithium of the Sn-doped  $\text{TiO}_2$ nts was evaluated by galvanostatic cycling experiments and compared to that of undoped  $\text{TiO}_2$ nts as shown in Fig. 9, with a summary also given in Table 3. In spite of the fact that both nanotubes (doped and undoped) were prepared under the same conditions (40 V in a viscous electrolyte consisting of 88.7 wt% glycerol, 1.3 wt%  $\text{NH}_4\text{F}$  and 10 wt%  $\text{H}_2\text{O}$ ), the Sn-doped  $\text{TiO}_2$ nts delivered much higher capacity values. It has already [30,60,61] been established that the reactivity of rutile  $\text{TiO}_2$  is sensitive to lithium diffusivity as a result of its peculiar crystal structure, hence the outstanding performance of the Sn-doped  $\text{TiO}_2$ nts is proposed to be related to the rutile-type structure and the enhanced lithium diffusivity imparted with the Sn doping; it was shown above with Cottrell plots (Fig. 8) that  $\text{Li}^+$  insertion into Sn-doped  $\text{TiO}_2$ nts is about 40 times faster than into undoped  $\text{TiO}_2$ nts. Also, cycling efficiencies were estimated to be 76%, 85% and 89% (Table 3) for the amorphous  $\text{TiO}_2$ nts, amorphous Sn-doped  $\text{TiO}_2$ nts and crystalline

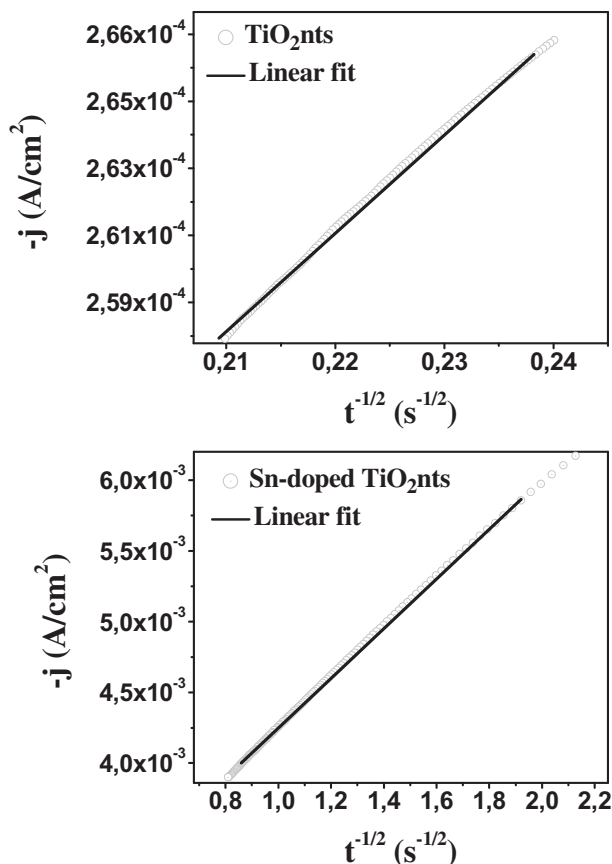


Fig. 8. Cottrell plots for the determination of  $\text{Li}^+$  diffusion coefficients in  $\text{TiO}_2\text{nts}$  and Sn-doped  $\text{TiO}_2\text{nts}$ .

Sn-doped  $\text{TiO}_2\text{nts}$  respectively. Cycling efficiency ( $E$ ) is a measure of capacity retention, and it can be expressed as the ratio of final reversible capacity ( $Q_f$ ) to initial reversible capacity ( $Q_i$ ) [13,14]. Generally, amorphous  $\text{TiO}_2$  electrodes exhibit lower cycling efficiencies than the crystalline counterparts, since the latter precludes lithium storage into defect sites and side reactions with substantial solvent traces [13]. Also, it can be asserted that so far as  $\text{TiO}_2$  electrodes are concerned, cycling efficiencies are somewhat sensitive to current densities (C-rate values) [13].

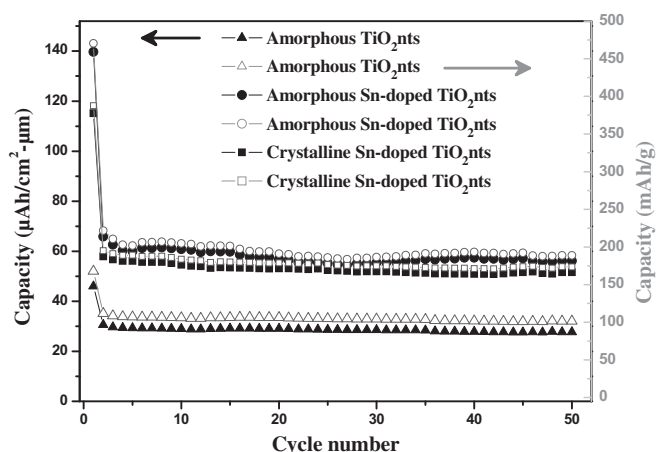


Fig. 9. Galvanostatic cycle life performance at  $70 \mu\text{A cm}^{-2}$  for the undoped and the Sn-doped  $\text{TiO}_2\text{nts}$  in the  $1.0 \leq U/V \leq 2.6$  voltage range. The capacity values are given in  $\mu\text{Ah cm}^{-2} \mu\text{m}^{-1}$  (closed symbols) and in  $\text{mAh g}^{-1}$  (open symbols) for amorphous  $\text{TiO}_2\text{nts}$  and Sn-doped  $\text{TiO}_2\text{nts}$  (amorphous and crystalline).

Table 3

Discharge capacities and cycling efficiencies (capacity retention) with  $70 \mu\text{A cm}^{-2}$  current density.

Electrode	Condition	1st reversible capacity ( $\mu\text{Ah cm}^{-2} \mu\text{m}^{-1}$ )	Irreversible capacity ( $\mu\text{Ah cm}^{-2} \mu\text{m}^{-1}$ )	50th reversible capacity ( $\mu\text{Ah cm}^{-2} \mu\text{m}^{-1}$ )	Cycling efficiency (%)
$\text{TiO}_2\text{nts}$	1–2.6 V	28.6	17.0	21.9	76
Sn-doped $\text{TiO}_2\text{nts}$	1–2.6 V	65.9	73.9	56.1	85
Sn-doped $\text{TiO}_2\text{nts}^a$	1–2.6 V	57.9	57.2	51.6	89

<sup>a</sup> Crystalline.

The reaction for the reversible insertion of lithium into  $\text{TiO}_2$  is as given in Eq. (5). Although a maximum of  $0.5 \text{ Li}^+$  can be inserted into anatase, rutile can host up to  $1 \text{ Li}^+$  (depending on the cut-off potential) of which almost  $0.5 \text{ Li}^+$  are irreversibly trapped in the structure during the first discharge [14,30]. Due to the degree of the Sn-doping, the Sn-doped  $\text{TiO}_2\text{nts}$  undergo full electrochemical reaction like a rutile-type  $\text{TiO}_2$  [29]. That is the reason for the very

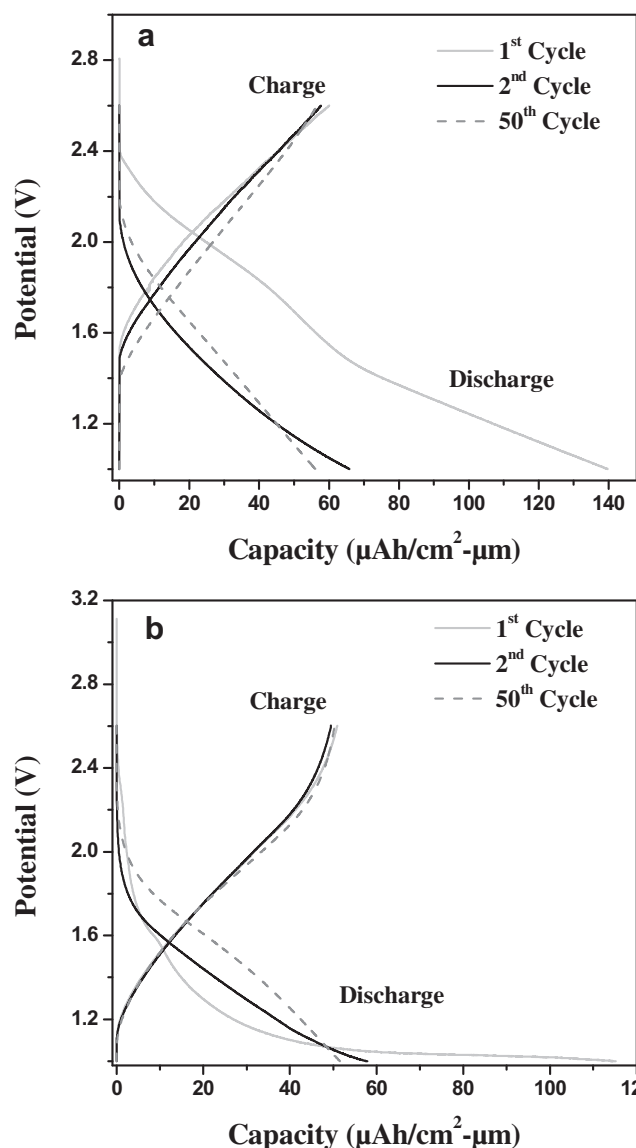
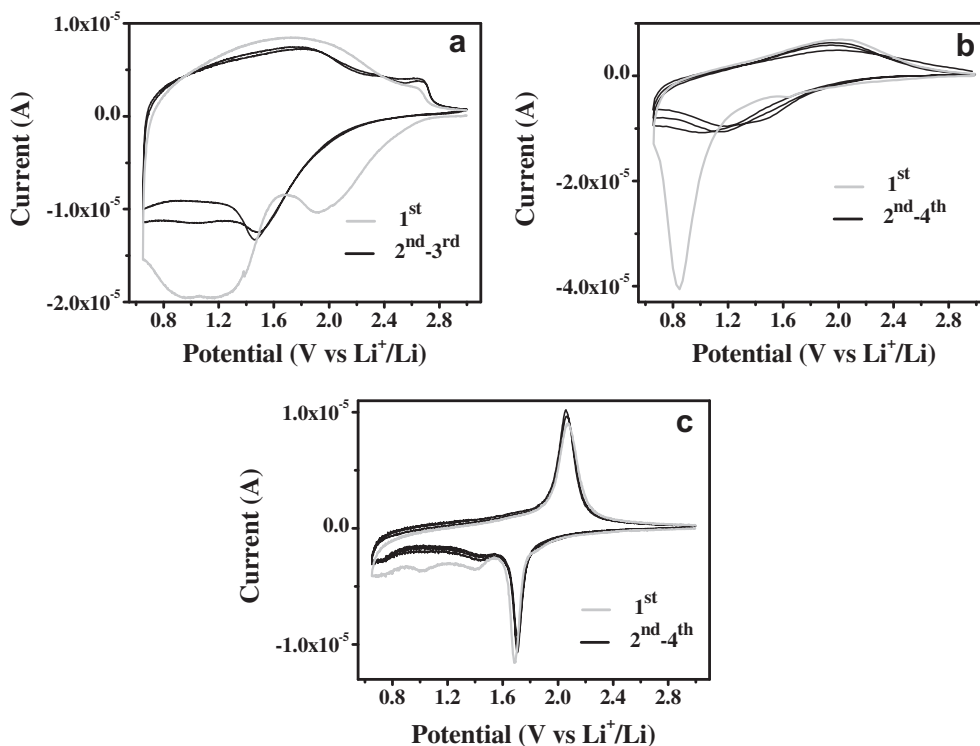
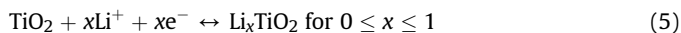


Fig. 10. Galvanostatic curves obtained for the Sn-doped  $\text{TiO}_2\text{nts}$  (a: amorphous, b: crystalline) cycled in the  $1.0 \leq U/V \leq 2.6$  voltage range.



**Fig. 11.** CV curves recorded at  $0.1 \text{ mV s}^{-1}$  in the  $0.65 \leq U/V \leq 3$  voltage range for Sn-doped  $\text{TiO}_2\text{nts}$  (a: amorphous; b: crystalline), and crystalline  $\text{TiO}_2\text{nts}$  (c).

high first discharge capacities ( $139.7 \mu\text{Ah cm}^{-2} \mu\text{m}^{-1}$  for amorphous, and  $115.1 \mu\text{Ah cm}^{-2} \mu\text{m}^{-1}$  for crystalline) observed for the Sn-doped  $\text{TiO}_2\text{nts}$ . It has already been established that despite a very thin or inexistent solid electrolyte interphase (SEI) layer on  $\text{TiO}_2$  electrodes, adsorbed solvents on surfaces of amorphous samples or crystallized water in the case of annealed samples contribute to the irreversibility in the first discharge [14]. The pronounced irreversible capacities observed for the Sn-doped  $\text{TiO}_2\text{nts}$  ( $73.9 \mu\text{Ah cm}^{-2} \mu\text{m}^{-1}$  for amorphous, and  $57.2 \mu\text{Ah cm}^{-2} \mu\text{m}^{-1}$  for crystalline) as compared to the undoped  $\text{TiO}_2\text{nts}$  ( $17.0 \mu\text{Ah cm}^{-2} \mu\text{m}^{-1}$ ) are a consequence of the extra lithium-ions irreversibly trapped in the rutile-type structure. The corresponding capacity values in  $\text{mAh g}^{-1}$  are also presented in Fig. 9.



The galvanostatic discharge/charge profiles of the Sn-doped  $\text{TiO}_2\text{nts}$  (both amorphous and crystalline) are given in Fig. 10; the sloping voltage profiles agree well with the cyclic voltammograms shown in Fig. 11a, b, and are consistent with previous reports in literature [62–64]. For the crystalline Sn-doped  $\text{TiO}_2\text{nts}$ , the small plateau at ca. 1.65 V in the first discharge (Fig. 11b) can be attributed to surface storage of lithium, the corresponding small cathodic peak was also evidenced at ca. 1.6 V vs  $\text{Li}^+/\text{Li}$  in the 1st cycle CV (Fig. 11b). Although the long sloping plateau (in the first discharge) starting at ca. 1.2 V ends at the cut-off potential of 1 V, the CV studies in the  $0.65 \leq U/V \leq 3$  voltage range showed that the plateau is actually centred at ca. 0.85 V, and its irreversibility in the subsequent cycles is as a consequence of the extensive lithium storage up to that potential and the concomitant irreversible structural transformations.

The CV obtained from crystalline  $\text{TiO}_2\text{nts}$  (Fig. 11c) was presented to showcase the marked difference in the electrochemical characteristics brought about by the Sn-doping. It is worth noting that amorphous samples of  $\text{TiO}_2$ -based electrodes generally do not reveal the characteristic peaks of reaction with lithium. The

reduction peak at ca. 1.7 V vs  $\text{Li}^+/\text{Li}$  (Fig. 11c) corresponds to lithium insertion (reversible  $\text{Li}^+$  extraction peak at ca. 2.0 V vs  $\text{Li}^+/\text{Li}$ ) into the anatase  $\text{TiO}_2$  structure [14,31] and the peaks seen at ca. 1.1 V and 1.4 V vs  $\text{Li}^+/\text{Li}$  (Fig. 11c) correspond to lithium insertion into the infinitesimal proportion of rutile  $\text{TiO}_2$  as detected by XRD (Fig. 3) [30,60].

In accounting for the improved behaviour of the Sn-doped  $\text{TiO}_2$  nanotubes, it is important to note that the response of only the  $\text{Sn}_3\text{Ti}_5$  thin-film versus lithium is negligible and besides, the thin film is not active within the cycling voltage range of  $1.0 \leq U/V \leq 2.6$  as it consists mainly of Sn as the active material [16,17,65]. Indeed, it is not the first time a beneficial effect of hetero-atoms is observed on the electrochemical behaviour of anode materials for Li-ion batteries [22,66].

#### 4. Conclusion

Highly-ordered Sn-doped  $\text{TiO}_2\text{nts}$  can be produced by anodic oxidation of co-sputtered Ti–Sn thin films in a viscous electrolyte consisting of 88.7 wt% glycerol, 1.3 wt%  $\text{NH}_4\text{F}$  and 10 wt%  $\text{H}_2\text{O}$ . X-ray photoelectron spectroscopy confirmed that the nanotubes are formed by substitution of  $\text{Sn}^{4+}$  for  $\text{Ti}^{4+}$  during the oxide formation, leading to  $\text{Ti}_{1-x}\text{Sn}_x\text{O}_2$ -type nanotubes with  $x = \sim 0.5$ . Due to the degree of the Sn doping, the usual anatase  $\text{TiO}_2$  nanotubes are transformed into a rutile-type  $\text{TiO}_2$  according to X-ray diffraction studies.  $^{119}\text{Sn}$  Mössbauer spectroscopy studies confirmed the pure metallic nature of the co-sputtered Ti–Sn thin films and evidenced the octahedral substitution of  $\text{Sn}^{4+}$  for  $\text{Ti}^{4+}$  in the  $\text{TiO}_2$  structure as there were no traces of cassiterite ( $\text{SnO}_2$ ) in the material. With current density of  $70 \mu\text{A cm}^{-2}$  (1 C) and cut-off potential of 1 V, Sn-doped  $\text{TiO}_2\text{nts}$  delivered much higher capacity values as compared to simple  $\text{TiO}_2\text{nts}$ . The outstanding performance is proposed to be related to the enhanced lithium diffusivity evidenced with Cottrell plots, and the rutile-type structure imparted with the Sn doping.

The electrochemical studies have demonstrated that TiO<sub>2</sub> nanotubes indeed have the potential to be employed as anodes for the design of high-performance 3D Li-ion micro batteries. Further characterization such as *ex-situ* <sup>119</sup>Sn Mössbauer spectroscopy and post-mortem XRD of cycled electrodes would be useful to confirm that the Ti<sub>1-x</sub>Sn<sub>x</sub>O<sub>2</sub>-type nanotubes indeed undergo lithium insertion as a rutile-type TiO<sub>2</sub>. This novel synthesis approach can be extended for Fe/Sb/Nb-doping of on-wafer (Si) TiO<sub>2</sub> nanotubes due to the usefulness of TiO<sub>2</sub> nanotubes and the need to tune their intrinsic properties by doping.

## Acknowledgements

We thank the French Ministry of Education and ANR JCJC MICROLIONH no.2010 910 01 for financial support.

## References

- [1] D. Golodnitsky, V. Yufit, M. Nathan, I. Shechtman, T. Ripenbein, E. Strauss, S. Menkina, E. Peled, J. Power Sources 153 (2006) 281–287.
- [2] J.B. Bates, N.J. Dudney, B.J. Neudecker, F.X. Hart, H.P. Jun, S.A. Hackney, J. Electrochem. Soc. 147 (2000) 59.
- [3] K. Kanehori, K. Matsumoto, K. Miyauchi, T. Kudo, Solid State Ionics 9/10 (1983) 1445.
- [4] R.W. Hart, H.S. White, B. Dunn, D.R. Rolison, Electrochem. Commun. 5 (2003) 120–123.
- [5] W. Lai, C.K. Erdonmez, T.F. Marinis, C.K. Bjune, N.J. Dudney, F. Xu, R. Wartena, Y.M. Chiang, Adv. Mater. 22 (2010) E139.
- [6] J.W. Long, B. Dunn, D.R. Rolison, H.S. White, Chem. Rev. 104 (2004) 4463–4492.
- [7] J.B. Bates, N.J. Dudney, K.A. Weatherspoon, US Patent.
- [8] B. Fleutot, B. Pecquenard, F. Le Cras, B. Delis, H. Martinez, L. Dupont, D. Guy-Bouysson, J. Power Sources 196 (2011) 10289–10296.
- [9] P.H.L. Notten, F. Roozeboom, R.A.H. Niessen, L. Baggetto, Adv. Mater. 19 (2007) 4564–4567.
- [10] Y.J. Park, K.S. Park, J.G. Kim, M.K. Kim, H.G. Kim, H.T. Chung, J. Power Sources 88 (2000) 250–254.
- [11] M. Kotobuki, Y. Suzuki, H. Munakata, K. Kanamura, Y. Sato, K. Yamamoto, T. Yoshida, J. Power Sources 195 (2011) 5784–5788.
- [12] Z.G. Lu, H. Cheng, M.F. Lo, C.Y. Chung, Adv. Funct. Mater. 17 (2007) 3885–3896.
- [13] G.F. Ortiz, I. Hanzu, P. Knauth, P. Lavela, J.L. Tirado, T. Djenizian, Electrochim. Acta 54 (2009) 4262–4268.
- [14] G.F. Ortiz, I. Hanzu, T. Djenizian, P. Lavela, J.L. Tirado, P. Knauth, Chem. Mater. 21 (2009) 63–67.
- [15] J. Song, M.-Z. Cai, Q.-F. Dong, M.-S. Zheng, Q.-H. Wu, S.-T. Wu, Electrochim. Acta 54 (2009) 2748–2753.
- [16] L. Bazin, S. Mitra, P.L. Taberna, P. Poizat, M. Gressier, M.J. Menu, A. Barnabé, P. Simon, J.M. Tarascon, J. Power Sources 188 (2009) 578–582.
- [17] G.F. Ortiz, I. Hanzu, P. Lavela, P. Knauth, J.L. Tirado, T. Djenizian, Chem. Mater. 22 (2010) 1926–1932.
- [18] G.F. Ortiz, I. Hanzu, P. Knauth, P. Lavela, J.L. Tirado, T. Djenizian, Electrochem. Solid State Lett. 12 (2009) A186–A189.
- [19] P. Poizat, S. Laruelle, S. Grugeon, L. Dupont, J.M. Tarascon, Nature 407 (2000) 496–499.
- [20] L. Taberna, S. Mitra, P. Poizat, P. Simon, J.M. Tarascon, Nat. Mater. 5 (2006) 567–573.
- [21] G.F. Ortiz, J.L. Tirado, Electrochem. Commun. 13 (2011) 1427–1430.
- [22] P. Lavela, N.A. Kyeremateng, J.L. Tirado, Mater. Chem. Phys. 124 (2010) 102–108.
- [23] M.S. Whittingham, F.R. Gamble, Mater. Res. Bull. 10 (1975) 363–371.
- [24] C. Navone, J.P. Pereira-Ramos, R. Baddour-Hadjean, R. Salot, J. Electrochem. Soc. 153 (2006) A2287–A2293.
- [25] A. Gies, B. Pecquenard, A. Benayad, H. Martinez, D. Gonbeau, H. Fuess, A. Levasseur, Thin Solid Films 516 (2008) 7271–7281.
- [26] N. Plylahan, N.A. Kyeremateng, M. Eyraud, F. Dumur, H. Martinez, L. Santinacci, P. Knauth, T. Djenizian, Nanoscale Res. Lett. 7 (2012) 349.
- [27] N.A. Kyeremateng, F. Dumur, P. Knauth, B. Pecquenard, T. Djenizian, C. R. Chimie (2012). <http://dx.doi.org/10.1016/j.crci.2012.05.002>.
- [28] N.A. Kyeremateng, F. Dumur, P. Knauth, B. Pecquenard, T. Djenizian, Electrochem. Commun. 13 (2011) 894–897.
- [29] N.A. Kyeremateng, V. Hornebecq, P. Knauth, T. Djenizian, Electrochim. Acta 62 (2012) 192–198.
- [30] P. Kubiak, M. Pfanztel, J. Geserick, U. Hörmann, N. Hüsing, U. Kaiser, M. Wohlfahrt-Mehrens, J. Power Sources 194 (2009) 1099–1104.
- [31] T. Djenizian, I. Hanzu, P. Knauth, J. Mater. Chem. 21 (2011) 9925–9937.
- [32] D. Gong, C.A. Grimes, O.K. Varghese, W.C. Hu, R.S. Singh, Z. Chen, E.C. Dickey, J. Mater. Res. 16 (2001) 3331–3334.
- [33] J.M. Macak, H. Tsuchiya, A. Ghicov, K. Yasuda, R. Hahn, S. Bauer, P. Schmuki, Curr. Opin. Solid State Mater. Sci. 11 (2007) 3–18.
- [34] Y.D. Premchand, T. Djenizian, F. Vacandio, P. Knauth, Electrochem. Commun. 8 (2006) 1840–1844.
- [35] T. Djenizian, I. Hanzu, Y.D. Premchand, F. Vacandio, P. Knauth, Nanotechnology 19 (2008) 205601.
- [36] A. Weibel, R. Bouchet, S.L.P. Savin, A.V. Chadwick, P.E. Lippens, M. Womes, P. Knauth, ChemPhysChem 7 (2006) 2377–2383.
- [37] F. Fresno, D. Tudela, J.M. Coronado, J. Soria, Catal. Today 143 (2009) 230–236.
- [38] M.G. Faba, D. Gonbeau, G. Pfisterguillouzo, J. Electron. Spectrosc. 73 (1995) 65–80.
- [39] J.-C. Dupin, D. Gonbeau, P. Vinatier, A. Levasseur, Phys. Chem. Chem. Phys. 2 (2000) 1319–1324.
- [40] C. Guimon, A. Gervasini, A. Auroux, J. Phys. Chem. B 105 (2001) 10316–10325.
- [41] A.R. Gonzalez-Elipio, G. Munuera, J.P. Espinos, J.M. Sanz, Surf. Sci. 220 (1989) 368–380.
- [42] M.C. Biesinger, L.W.M. Lau, A.R. Gerson, R.S.C. Smart, Appl. Surf. Sci. 257 (2010) 887–898.
- [43] J.C. Parlebas, M.A. Khan, T. Uozumi, K. Okada, A. Kotani, J. Electron. Spectrosc. 71 (1995) 117–139.
- [44] J.L. Guimaraes, M. Abbate, S.B. Betim, M.C.M. Alves, J. Alloy. Compd. 352 (2003) 16–20.
- [45] D.K.G. Deboer, C. Haas, G.A. Sawatzky, Phys. Rev. B 29 (1984) 4401–4419.
- [46] I. Pollini, A. Mosser, J.C. Parlebas, Phys. Rep. 355 (2001) 1–72.
- [47] A.E. Bocquet, T. Mizokawa, K. Morikawa, A. Fujimori, S.R. Barman, K. Maiti, D.D. Sarma, Y. Tokura, M. Onoda, Phys. Rev. B 53 (1996) 1161–1170.
- [48] X.J. Zhu, Z.P. Guo, P. Zhang, G.D. Du, C.K. Poh, Z.X. Chen, S. Li, H.K. Liu, Electrochim. Acta 55 (2010) 4982–4986.
- [49] X. Zhou, W. Fu, H. Yang, D. Ma, J. Cao, Y. Leng, J. Guo, Y. Zhang, Y. Sui, W. Zhao, M. Li, Mater. Chem. Phys. 124 (2010) 614–618.
- [50] J.W. O'Brien, R.A. Dunlap, J.R. Dahn, J. Alloy. Compd. 353 (2003) 60–64.
- [51] J.W. O'Brien, R.A. Dunlap, J.R. Dahn, J. Alloy. Compd. 353 (2003) 65–73.
- [52] B. Grzeta, E. Tkalec, C. Goebbert, M. Takeda, M. Takahashi, K. Nomura, M. Jaksic, J. Phys. Chem. Solids 63 (2002) 765–772.
- [53] V.S. Urusov, D.A. Khramov, K. Langer, Eur. J. Mineral. 11 (1999) 295–298.
- [54] I. Issac, M. Scheuermann, S.M. Becker, E.G. Bardaji, C. Adelhelm, D. Wang, C. Kuebel, S. Indris, J. Power Sources 196 (2011) 9689–9695.
- [55] L. Aldon, P. Kubiak, A. Picard, J.C. Jumas, J. Olivier-Fourcade, Chem. Mater. 18 (2006) 1401–1406.
- [56] L.V. Taveira, A.A. Saguees, J.M. Macak, P. Schmuki, J. Electrochem. Soc. 155 (2008) C293–C302.
- [57] I. Hanzu, T. Djenizian, P. Knauth, J. Phys. Chem. C 115 (2011) 5989–5996.
- [58] I. Hanzu, T. Djenizian, G.F. Ortiz, P. Knauth, J. Phys. Chem. C 113 (2009) 20568–20575.
- [59] L. Kavan, M. Grätzel, S.E. Gilbert, C. Klemen, H.J. Scheel, J. Am. Chem. Soc. 118 (1996) 6716–6723.
- [60] M. Pfanztel, P. Kubiak, M. Fleischhammer, M. Wohlfahrt-Mehrens, J. Power Sources 196 (2011) 6815–6821.
- [61] W.J. Macklin, R.J. Neat, Solid State Ionics 53–56 (1992) 694–700.
- [62] H. Uchiyama, E. Hosono, H. Zhou, H. Imai, Solid State Ionics 180 (2009) 956–960.
- [63] S. Dong, H. Wang, L. Gu, X. Zhou, Z. Liu, P. Han, Y. Wang, X. Chen, G. Cui, L. Chen, Thin Solid Films 519 (2011) 5978–5982.
- [64] J.S. Chen, X.W. Lou, J. Power Sources 195 (2010) 2905–2908.
- [65] G.F. Ortiz, P. Lavela, P. Knauth, T. Djenizian, R. Alcantara, J.L. Tirado, J. Electrochem. Soc. 158 (2011) A1094–A1099.
- [66] M.J. Aragon, B. Leon, T. Serrano, C.P. Vicente, J.L. Tirado, J. Mater. Chem. 21 (2011) 10102–10107.